Monthly Notices
of the
ROYAL ASTRONOMICAL SOCIETY

MNRAS **00,** 1 (2020)
Advance Access publication 2020 February 20

doi:10.1093/mnras/staa508

How comets work: nucleus erosion versus dehydration

Marco Fulle [1]★ J. Blum,[2] A. Rotundi,[3,4] B. Gundlach,[2] C. Güttler [5] and V. Zakharov[3]

[1]*INAF – Osservatorio Astronomico, Via Tiepolo 11, I-34143 Trieste, Italy*
[2]*Institut für Geophysik und extraterrestrische Physik, Technische Universität Braunschweig, Mendelssohnstrße 3, D-38106 Braunschweig, Germany*
[3]*INAF – Istituto di Astrofisica e Planetologia Spaziali, Via Fosso del Cavaliere 100, I-00133 Rome, Italy*
[4]*Universitá degli Studi di Napoli Parthenope, Dip. di Scienze e Tecnologie, CDN IC4, I-80143 Naples, Italy*
[5]*Max-Planck-Institut für Sonnensystemforschung, Justus-von-Liebig-Weg 3, D-37077 Göttingen, Germany*

Accepted 2020 February 17. Received 2020 February 15; in original form 2019 December 16

ABSTRACT

We develop an activity model based on ice sublimation and gas diffusion inside cm-sized pebbles making-up a cometary nucleus. Our model explains cometary activity assuming no free parameters and fixing the nucleus surface temperature T_s, its gradient below the nucleus surface at thermal equilibrium, the pressure inside the porous pebbles, and the gas flux from them. We find that (i) the nucleus erosion rate and water vapour flux are independent of the nucleus refractory-to-ice ratio, which affects the dehydration rate only; (ii) water-driven dust ejection occurs in thermal quasi-equilibrium at $T_s > 205$ K; (iii) the smallest and largest ejected dust sizes depend on the nucleus surface temperature and its gradient at depths of few cm; and (iv) the water-driven nucleus erosion rate is independent of the water vapour flux. Regarding comet 67P/Churyumov–Gerasimenko, we find that (i) during the northern and southern polar summers, the nucleus active areas are $\approx$5 km^2; (ii) >95 per cent of the southern pristine nucleus has a refractory-to-water-ice mass ratio >5; and (iii) the different temperature dependences of the dehydration and erosion rates explain the seasonal cycle: at perihelion, dm-sized chunks ejected by the sublimation of CO_2 ices are rapidly enveloped by an insulating crust, preserving most water ice up to their fallout on the northern dust deposits; the inbound water-driven activity at low temperatures triggers a complete erosion of the fallout if its water-ice mass fraction is >0.1 per cent.

Key words: comets: general – comets: individual: 67P/Churyumov–Gerasimenko.

1 INTRODUCTION

Many data provided by the *Rosetta* mission at comet 67P/Churyumov–Gerasimenko (67P hereafter) are challenging the available thermophysical models of cometary activity (Keller et al. 2015; Blum et al. 2017; Hu et al. 2017). The observed 67P seasonal cycle (Keller et al. 2017; Fulle et al. 2019a) includes the ejection of chunks larger than the water-ice sublimation front (Fulle et al. 2016; Ott et al. 2017; Pajola et al. 2017; Gundlach, Fulle & Blum 2020). The negligible disintegration of chunks at perihelion during their flight towards the fallout into the northern deposits (Biver et al. 2019) seems inconsistent with the inbound activity observed in Hapi, a fallout deposit most active in 2014 August (Keller et al. 2017). Hapi's erosion has been measured (Cambianica et al. 2020) at rates about two orders of magnitude faster than predicted (Keller et al. 2015). An activity model consistent with the available 67P data is needed to combine the high refractory-to-ice mass ratio of cometary nuclei (Fulle et al. 2017; Cambianica et al. 2020) with their activity lasting many orbits.

These challenges are probably connected with two activity paradoxes affecting all the available thermophysical models: (i) How is it possible that water-ice sublimation from the nucleus surface does not lead to an insulating crust, inhibiting gas and dust ejection (Kührt and Keller 1994; Blum et al. 2014)? (ii) How is it possible that the gas, flowing through the nucleus surface with a pressure <1 Pa at perihelion (Pajola et al. 2017), ejects dust particles whose tensile strengths are >10 Pa (Skorov and Blum 2012; Gundlach et al. 2015; Güttler et al. 2019)? Fulle, Blum & Rotundi (2019b) have shown that possible answers to these questions are provided by water-ice sublimation and gas diffusion inside the cm-sized pebbles making-up cometary nuclei (Blum et al. 2017). In this paper, we improve such a gas diffusion model fixing in a self-consistent approach both the gas pressure inside the pebbles and the gas flux driving its diffusion inside the porous pebbles. This model allows us to define a nucleus erosion independent of its dehydration, and overcomes all the challenges listed above.

2 GAS DIFFUSION INSIDE THE PEBBLES

We assume that the pebbles making-up cometary nuclei are non-homogeneous aggregates of ice and dust particles characterized

★ E-mail: fulle@oats.inaf.it

by the size distribution measured by *Rosetta* at 67P, namely a power law with the differential index -3 ± 1 (Blum et al. 2017). Gas diffusion is driven by the pores among the particles making-up the pebbles (Figs 1 and 2), rather than by the pores among the grains (named also monomers in Güttler et al. 2019) making-up each particle (Fulle et al. 2019b). A homogeneous agglomerate of monomers all of the same size has the average pore radius equal to the 20 per cent of the monomer diameter (Fulle et al. 2019b). In order to compute the pore size distribution in realistic pebbles composed of dust particles of sizes ranging from the grain one to the pebble one, we performed many random packing simulations both in 3D and in 2D, which has the big advantage to be easily plotted (Figs 1 and 2). A dust size distribution with power index -3 in the 3D space corresponds to a size distribution with power index -2 in the 2D space: the largest particles dominate both the volume in the former and the area in the latter. In both 3D and 2D simulations, the pore distribution is steeper than that of the particles making-up the pebble (Figs 1 and 2). Moreover, the higher the number of small particles filling the voids among big particles, the steeper the pore size distribution, i.e. the pebble porosity tends towards the individual particle porosity. The pore radius distribution is

$$p(a)\,\mathrm{d}a = \frac{(\alpha-1)\,a_\mathrm{m}^{\alpha-1}}{1-(a_\mathrm{m}/a_\mathrm{M})^{\alpha-1}}\,a^{-\alpha}\,\mathrm{d}a, \tag{1}$$

$$\int_{a_\mathrm{m}}^{a_\mathrm{M}} p(a)\,\mathrm{d}a = 1, \tag{2}$$

where a_m and a_M are the minimum and maximum pore radii, respectively, and $-\alpha$ is the power index of the pore size distribution, with $\alpha \geq 3$ according to the performed 2D and 3D computations (see Figs 1 and 2). Since $a_\mathrm{m} \ll a_\mathrm{M}$, the gas diffusivity, D_G, becomes

$$D_\mathrm{G} = \frac{4}{3}\sqrt{\frac{2kT}{\pi m}}\int_{a_\mathrm{m}}^{a_\mathrm{M}} a\,p(a)\,\mathrm{d}a \approx \frac{4(\alpha-1)\,a_\mathrm{m}}{3(\alpha-2)}\sqrt{\frac{2kT}{\pi m}}, \tag{3}$$

i.e. at most a factor of 2 larger than in the homogeneous case (Fulle et al. 2019b). Here, T is the pebble temperature, k the Boltzmann constant, m the water molecule mass, and $a_\mathrm{m} = 20$ nm is the average radius of the pores among the smallest possible dust particles, i.e. the monomers.

Along the radial coordinate r inside the pebble of radius $R \approx 5$ mm (Blum et al. 2017), the gas pressure inside the pebbles due to

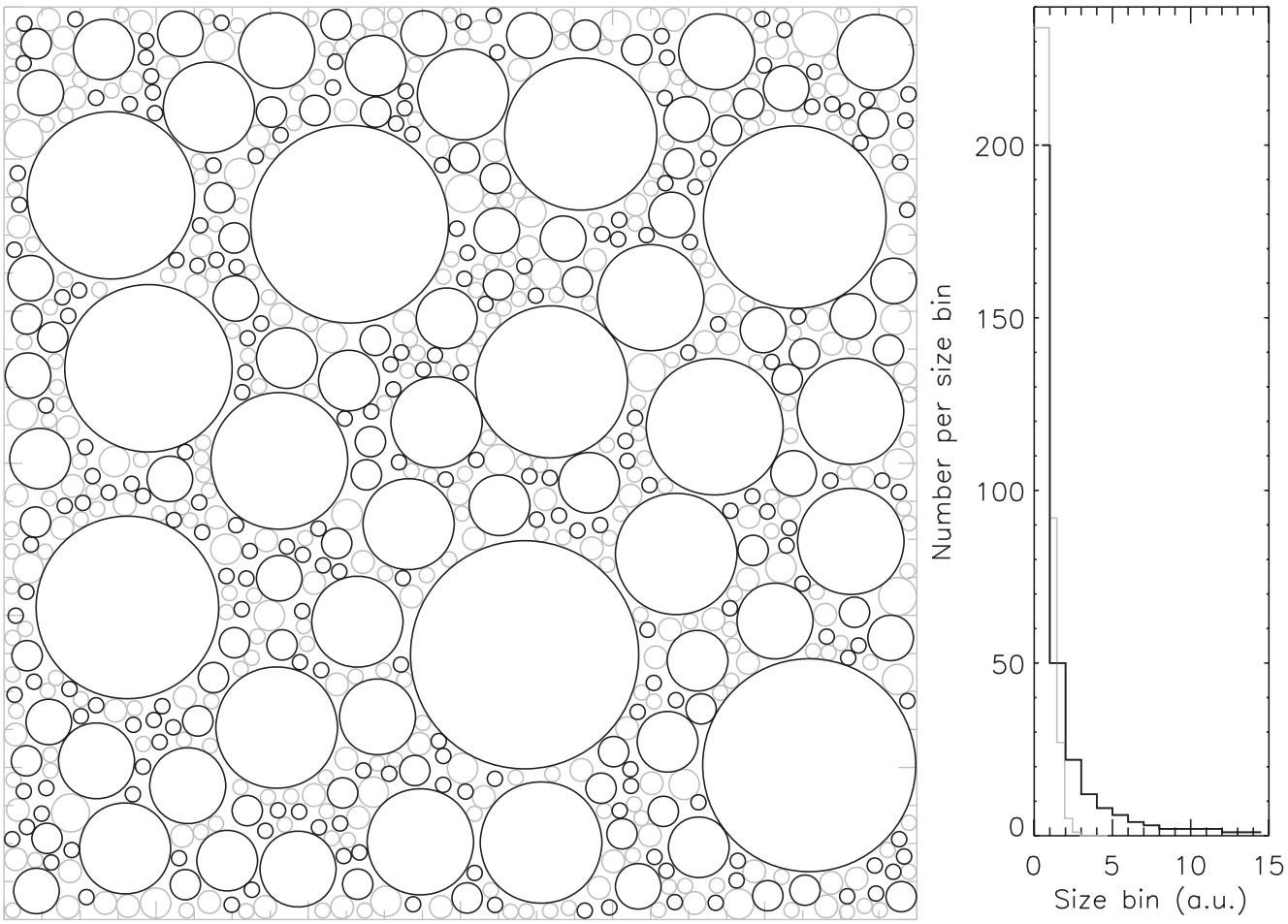

Figure 1. Subset of a non-homogeneous 2D loose-packed pebble composed of dust particles (black circles, left-hand panel) characterized by the differential size distribution with power index -2 (black histogram, right-hand panel). The largest possible circles filling the voids among dust particles define the pores (grey circles, left-hand panel) characterized by a steeper size distribution (grey histogram, right-hand panel) with power index ≈ -4. Pores smaller than the smallest dust particles are not shown in this case. 3D models of close-packed spheres with a power index of -3 of the differential size distribution provide a steeper pore size distribution (power index ≈ -6).

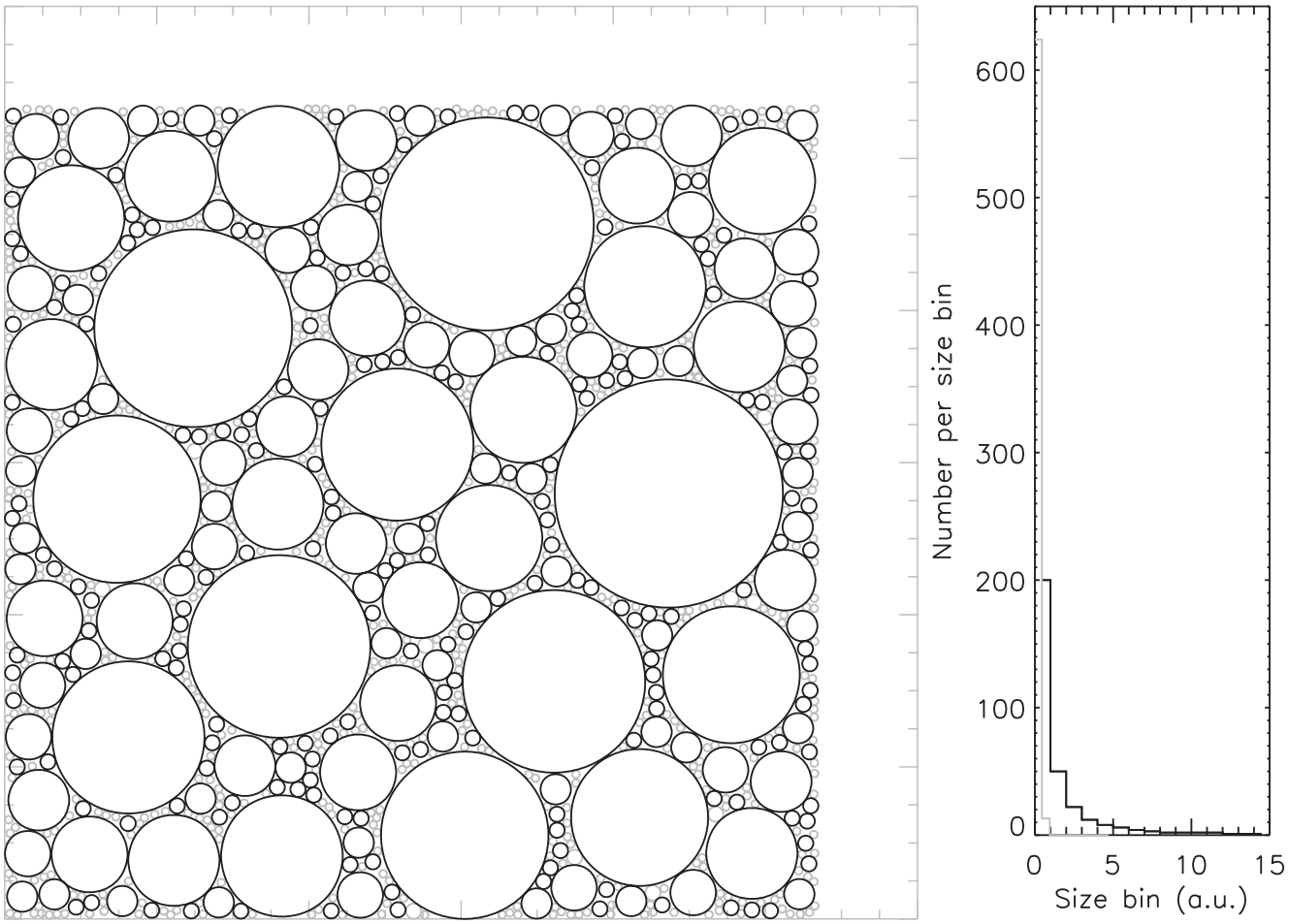

Figure 2. Subset of a non-homogeneous 2D close-packed pebble composed of dust particles (black circles, left-hand panel) characterized by the differential size distribution with power index −2 (black histogram, right-hand panel). In this case, the pore size distribution (grey circles and histogram) has a power index ≈−5. Also in these close packings, the number of contact points bonding the superficial dust particles to the pebble is lower than in the homogeneous case. For instance, the largest particle at the lower surface (left-hand panel, centre-bottom) is connected to the pebble through a single contact with the particle to its lower left, and then to the pebble centre through a continuous sequence of contact points among neighbours. The other contacting particles to the lower right are disconnected from the pebble and will be ejected together with the superficial particle if their sizes are $s < s_\mathrm{m}$. Few contacts among particles characterize also 3D close packing of spheres with a power index of the differential size distribution of −3, where small spheres are too few to fill all available voids.

the gas diffusion is (Fulle et al. 2019b)

$$P(T,r) = P_\mathrm{out} + \frac{3\,(\alpha-2)\,Q(T)\,R}{16\,(\alpha-1)\,a_\mathrm{m}}\left[1-\left(\frac{r}{R}\right)^4\right]\sqrt{\frac{\pi kT}{2m}}, \quad (4)$$

where $Q(T)$ is the gas flux from the pebbles on the nucleus surface and P_out is the gas pressure among the pebbles.

The average pressure $P(T)$ inside the pebble is

$$P(T) = \frac{4\pi}{\frac{4}{3}\pi R^3}\int_0^R P(T,r)\,r^2\,\mathrm{d}r = P_\mathrm{out} + \frac{3Q(T)R}{35a_\mathrm{m}}\sqrt{\frac{\pi kT}{2m}}, \quad (5)$$

with $\alpha = 6$ provided by the performed 3D computation of random close packing of spheres with a power index of their differential size distribution of −3. Here we consider only pressures $P(T) - P_\mathrm{out} \geq 0.1$ Pa. According to the model of a pebble-made nucleus (Blum et al. 2017), $P_\mathrm{out} \ll 0.1$ Pa, so that P_out can be neglected hereafter (see the actual values of P_out at the end of this section).

The water-ice sublimates inside the pebble, so that

$$Q(T) = \left[P_0\,\mathrm{e}^{-T_0/T} - P(T)\right]\sqrt{\frac{m}{2\pi kT}}, \quad (6)$$

with $P_0 = 3.23 \times 10^{12}$ Pa and $T_0 = 6134.6$ K (Gundlach, Skorov & Blum 2011). The pressure $P(T)$ in equations (5) and (6) is the same, because the pressure dumping the sublimation of water ice is exactly the ambient pressure inside the pebble provided by the gas diffusion inside it. Equations (5) and (6) can then be coupled to provide both $P(T)$ and $Q(T)$, namely

$$\left[\frac{3R}{70a_\mathrm{m}} + 1\right] Q(T) = P_0\,\mathrm{e}^{-T_0/T}\sqrt{\frac{m}{2\pi kT}}. \quad (7)$$

Within a relative error $\frac{70a_\mathrm{m}}{3R} \approx 0.01$ per cent, $P(T)$ becomes

$$P(T) \approx P_0 \exp\left[-\frac{T_0}{T}\right]. \quad (8)$$

$P(T)$ strongly increases as the temperature T slightly increases. Equilibrium thermal conditions are reached in ≤2 h of constant insolation (Fulle et al. 2019b), occurring e.g. in the northern and southern polar summers, and provide the highest possible T values, allowing us to neglect pressures far from equilibrium. Every thermal

profile at depths of a few cm has an average thermal gradient, so that the temperature T can be approximated to

$$T = T_s - s\,\nabla T, \tag{9}$$

where T_s is the temperature of the nucleus surface, s is the depth below the nucleus surface, and ∇T is the average gradient of the temperature at the equilibrium for $P(T) \geq 0.1$ Pa, i.e. $T > 195$ K according to equation (8). The temperature T_s is either provided by observations (Tosi et al. 2019), or computed by means of the energy balance equation

$$(1 - A)\,I_\odot \cos\theta\, r_h^{-2} = \epsilon\sigma T_s^4 + \lambda_s(T)\,\nabla T + \Lambda\, Q(T), \tag{10}$$

where $A = 1.2$ per cent is the nucleus Bond albedo (Fornasier et al. 2015), $I_\odot$ is the solar flux at the Earth heliocentric distance, θ is the solar zenithal angle, r_h is the nucleus heliocentric distance in astronomical units, $\epsilon \approx 0.9$ is the emissivity, σ is the Stefan–Boltzmann constant, $\lambda_s(T)$ is the heat conductivity inside the nucleus, and $\Lambda = 2.86 \times 10^6$ J kg^{-1} is the latent heat of sublimation of water ice (Orosei et al. 1995). At thermal equilibrium, ∇T is provided by (Blum et al. 2017)

$$\frac{\mathrm{d}}{\mathrm{d}s}\lambda_s(T)\nabla T = (\nabla T)^2 \frac{\mathrm{d}\lambda_s(T)}{\mathrm{d}T} = q\,\Lambda\,Q(T), \tag{11}$$

where q is the surface-to-volume ratio at sublimation, occurring in a uniform layer of thickness $2R$ of randomly packed pebbles, so that q is best approximated by the surface-to-volume ratio of a cube of edge $2R$, i.e. $q = (2R)^{-1}$. In a pebble-made nucleus, the heat conductivity is dominated by the radiation among the pebbles (Blum et al. 2017),

$$\lambda_s(T) \approx \frac{32}{3}\,\sigma\,R\,T^3, \tag{12}$$

assuming a pebble porosity of 60 per cent. Equations (11) and (12) give

$$\nabla T = \frac{\sqrt{\Lambda\,Q(T_s - R\,\nabla T)/\sigma}}{8(T_s - R\,\nabla T)\,R}, \tag{13}$$

so that equations (7) and (8) become

$$Q(s) = \frac{35 a_m\,P(s)}{3R}\sqrt{\frac{2m}{\pi k\,(T_s - s\,\nabla T)}}, \tag{14}$$

$$P(s) \approx P_0\,f(s)\exp\left[-\frac{T_0}{T_s - s\,\nabla T}\right], \tag{15}$$

where $f(s) = 1 - (1 - \frac{s}{R})^4$ for $s \leq R$ given by equation (4). For $s \geq R$, $f(s) = 1$ because pebble centres are located at every depth s, due to the random packing of pebbles. Equations (10), (12), (13), and (14) must be solved altogether, fixing T_s, ∇T, λ_s, and $Q(R) = Q$. Equation (15) is plotted in Fig. 3 for the obtained solutions at perihelion ($T_s = 300$ K, $\nabla T = 50$ K cm^{-1}, $Q = 7 \times 10^{-5}$ kg m^{-2} s^{-1}, $\lambda_s = 6 \times 10^{-2}$ W m^{-1} K^{-1}) and in 2014 August ($T_s = 220$ K, $\nabla T = 4$ K cm^{-1}, $Q = 2.3 \times 10^{-7}$ kg m^{-2} s^{-1}, $\lambda_s = 3 \times 10^{-2}$ W m^{-1} K^{-1}), with $T_s = 220$ K measured in Hapi by the Visible and InfraRed Thermal Imaging Spectrometer (VIRTIS) instrument (Tosi et al. 2019). Since $Q(s)$ depends linearly on $P(s)$ and in equation (5) is approximated to the average Q in each superficial pebble, $|P(s) - P(R)|/P(R)$ for $1 \leq s \leq 10$ mm provides the error affecting Q, which is 20 per cent in 2014 August, and 90 per cent at perihelion. The errors affecting ∇T are always $\leq$40 per cent, and $\leq$10 K for T_s. Within these uncertainties, the obtained values of T_s and ∇T fit those computed by other thermal models (Schloerb et al. 2015; Blum et al. 2017) and, at perihelion, those of time-dependent thermal models (Gundlach et al. 2020).

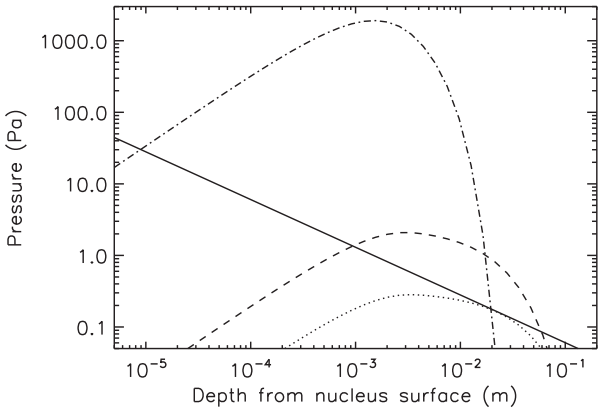

Figure 3. Pressure P inside the pebbles versus the depth s. Continuous line: tensile strength S bonding a homogeneous aggregate of dust grains (Skorov and Blum 2012; Güttler et al. 2019). Dashed–dotted line: P at $T_s = 300$ K and $\nabla T = 50$ K cm^{-1} crosses S at $s_m = 10$ μm and $s_M = 2$ cm. Dashed line: P at $T_s = 220$ K and $\nabla T = 4$ K cm^{-1} crosses S at $s_m = 1$ mm and $s_M = 6$ cm. Dotted line: P at $T_s = 205$ K, $\nabla T = 2$ K cm^{-1}, and $Q = 4 \times 10^{-8}$ kg m^{-2} s^{-1} is tangent to S at $s_m = s_M = 2$ cm. For every T_s, the nucleus at the depth s_M maintains a temperature $T_s - \nabla T\,s_M \approx 200$ K.

Equation (15) provides the gas pressure inside the pebbles only. Outside, the pressure P_{out} is much lower than inside, because the gas leaves the nucleus through the macropores among the pebbles, so that equation (15) does not imply any inward gas flux. P_{out} is given by (Blum et al. 2017)

$$P_{out} = \left[1 - \left(1 + \frac{s}{14R}\right)^{-1}\right] Q(s)\,\sqrt{2\pi k\,(T_s - s\,\nabla T)/m}, \tag{16}$$

providing $P_{out} \leq 5 \times 10^{-3}$ Pa at perihelion, and $P_{out} \leq 10^{-5}$ Pa in 2014 August.

3 EROSION VERSUS DEHYDRATION

The observed 67P dust volume distribution has a peak at 0.2 m (Fulle et al. 2016, 2019a; Ott et al. 2017; Pajola et al. 2017), so that in each pebble smaller particles are too few to fill all the voids among larger particles (Fig. 2). Many performed 3D random packing computations of particles with a power index of their size distribution equal to -3 show that the number of contact points bonding a superficial particle of a size s to the pebble is lower than in homogeneous agglomerates composed of particles all of that size s, with the tensile strength, S, bonding the superficial dust particles to the pebble $S = 13 s^{-2/3}$ mPa (Skorov and Blum 2012, with s in metres, Fig. 3). Since dust is ejected always from the nucleus surface, we can identify the dust size with the depth s. Dust is ejected when $T_s > 205$ K (P curve tangent to S line in Fig. 3), consistent with 67P activity onset in 2014 April (Moreno et al. 2017) and with Hapi's $215 < T_s < 225$ K measured by VIRTIS in 2014 August (Tosi et al. 2019). $P \geq S$ defines the minimum, s_m, and maximum, s_M, ejected dust sizes. When $s < 2R$, dust particles leave the surface of the superficial pebbles. When $s > 2R$, clusters of pebbles and particles are detached from the pebbles underneath. When the cluster has a size $s > s_M$, it is named chunk.

The 67P dust volume distribution implies that the erosion depends on the frequency at which the largest particles, of size $s_M < 0.2$ m, are ejected. During the nucleus erosion, the pebbles underneath,

suddenly exposed to sunlight, have a temperature $T_s - \nabla T\, s_M \approx$ 200 K (Fig. 3) for all values of T_s. The nucleus at the depth s_M maintains the same temperature regardless of the strong increase of T_s. All available Microwave Instrument for the *Rosetta* Orbiter (MIRO) and VIRTIS thermal data (Gulkis et al. 2015; Schloerb et al. 2015; Tosi et al. 2019), as well as all nucleus thermal models (De Sanctis et al. 2015; Schloerb et al. 2015; Blum et al. 2017; Hu et al. 2017; Tosi et al. 2019; Gundlach et al. 2020), confirm such an increasing dumping of e.g. diurnal thermal waves as the depth increases. Hence, dust ejection occurs in quasi-equilibrium thermal conditions, and the nucleus erosion rate, E, is given by the size s_M divided by the heat conduction time-scale $\rho_d c_p s_M^2/\lambda_s(s_M)$,

$$E = \frac{\lambda_s(s_M)}{\rho_d\ c_p\ s_M}, \tag{17}$$

where $\rho_d \approx 800$ kg m^{-3} is the average bulk density of the dust particles (Fulle et al. 2017), $c_p \approx 10^3$ J kg^{-1} K^{-1} is the heat capacity of the pebbles (Blum et al. 2017), and $\lambda_s(s_M) = 2.4 \times 10^{-2}$ W m^{-1} K^{-1} is the heat conductivity of the nucleus at the depth s_M, i.e. at $T \approx 200$ K.

The nucleus dehydration rate, D, is given by

$$D = \frac{(1+\delta)\ Q}{\rho_n}, \tag{18}$$

where δ is the average refractory-to-water-ice mass ratio in the nucleus and $\rho_n = 538$ kg m^{-3} is the nucleus average bulk density (Pätzold et al. 2019). When $D < E$, the water-driven activity does never stop, because the vapour diffusion erodes the surface pebbles before they become dry, exposing the underlying ice-rich ones. On the contrary, when $D > E$, the water-driven activity stops, because the dehydration builds-up an insulating crust of dried pebbles before being eroded by the dust ejection, driven by the heat conduction.

4 DISCUSSION

In 2014 August $T_s = 220$ K (Tosi et al. 2019) and $s_M = 6$ cm (Fig. 3), which in equation (17) gives $E = 4.3$ cm d^{-1}. This dust was probably ejected from Hapi, so that equation (17) predicts Hapi's observed erosion rate of 6 ± 2 cm d^{-1} (Cambianica et al. 2020). $Q = 2.3 \times 10^{-7}$ kg m^{-2} s^{-1} in equation (18) gives $D < 4$ cm d^{-1} for $\delta < 10^3$, so that $D < E$. The water-driven activity is not stopped by Hapi's very low ice mass fraction: it stops either when all Hapi's fallout from the previous perihelion has been completely eroded (Cambianica et al. 2020) or when a dry crust of thickness $>s_M$ inhibits the dust ejection. The water-vapour-loss rate measured in 2014 August of 1.2 kg s^{-1} (Gulkis et al. 2015) constrains the nucleus area involved in the water-driven erosion to $\approx$5 km^2, about twice Hapi's surface (Thomas et al. 2018), and provides a maximum liftable size $<s_m \approx 1$ mm (Fig. 3) from a spherical nucleus of 67P mass (Zakharov et al. 2018). If all the thermal energy of the gas at the pressure P in the volume enveloping the dust particle ($<$1/6 of the particle volume) is transferred to the dust kinetic energy, then dust is ejected with a velocity $<\sqrt{(P-S)/\rho_d}$. Therefore, all the eroded dust will reach a height $<$5 m before falling back on the nucleus. The maximum escaping dust size depends on the local gas density above the nucleus surface, which decreases as the gas expands (e.g. above a spherical nucleus as assumed by Zakharov et al. 2018), but on the opposite increases above nucleus concavities. Therefore, a negligible fraction of the eroded particles may escape the nucleus from Hapi, above which the nucleus has the hugest concavity, thus making the observed erosion $E = 6 \pm 2$ cm d^{-1} (Cambianica et al. 2020) consistent with the observed dust-loss rate $Q_d \approx 7$ kg s^{-1} (Rotundi et al. 2015). This fact also explains why the computed value of s_M is a factor of 3 larger than the largest size observed in 67P coma in 2014 August (Rotundi et al. 2015): the bigger the particles, the more probable that all fall back on the nucleus. Also the computed value of s_m is a factor of 5 larger than the smallest particles observed in 67P coma in 2014 August (Rotundi et al. 2015; Fulle et al. 2019b). The values of S and s_m may be overestimated, because the performed 3D random packing computations provide a number of contact points between a particle and the pebble between 2 and 4, whereas they are $\geq$4 in homogeneous aggregates.

At perihelion $T_s = 300$ K provides $s_m = 10$ μm (Fig. 3), consistent with perihelion dust data (Fulle et al. 2019b; Güttler et al. 2019), and $s_M = 2$ cm. Equation (17) provides $E = 13$ cm d^{-1}, which fits the dust-loss rate $Q_d \approx 260$ kg s^{-1} measured in the size range $s_m \leq s \leq s_M$ (Fulle et al. 2016) if the eroded nucleus surface is $Q_d c_p s_M/\lambda_s(s_M) \approx 0.2$ km^2. This area is much smaller than the nucleus area of $\approx$5 km^2 making the computed $Q = 7 \times 10^{-5}$ kg m^{-2} s^{-1} consistent with the perihelion water-loss rate of $\approx$350 kg s^{-1} (Shinnaka et al. 2017; Biver et al. 2019; Fulle et al. 2019a). Also the area ejecting chunks of size $s > s_M$ by CO_2, which cannot eject dust because its sublimation front is at a depth $s > s_M$, is $\approx$5 km^2 (Gundlach et al. 2020). The computed value of Q provides a maximum liftable size of $\approx$0.1 m (Zakharov et al. 2018), so that most ejected dm-sized chunks fall back on the Northern hemisphere (Fulle et al. 2019a), whereas all the dust with $s_m \leq s \leq s_M$ is surely lost in space. Equation (18) gives $D < 13$ cm d^{-1} for $\delta < 5$, taking into account the uncertainty affecting Q. It follows that dust and chunks may be ejected from different nucleus areas. In the $\approx$0.2 km^2 where $\delta < 5$, we have $D < E$, so that the nucleus erosion into dust exposes ice-rich pebbles sustaining the water-ice sublimation. On the contrary, the $\approx$5 km^2 ejecting dm-sized chunks by CO_2 activity (Gundlach et al. 2020) cannot eject dust, otherwise Q_d would be a factor of 20 larger than observed: this area must then have $\delta > 5$, so that $D > E$ and the nucleus erosion into dust stops. However, the ejection of dm-sized chunks exposes pebbles with some ice inside (according to the actual value of $\delta > 5$), so that water-ice sublimation is sustained by the nucleus erosion into chunks, rather than into dust. Since some dust is ejected by chunk-erosion-driven water-ice sublimation (occurring during the making of a crust because $D > E$), the area of $\delta < 5$ may be $\ll$0.2 km^2, because the area of $\delta > 5$ is a factor of $>$20 larger. It follows that the ejected chunks must have $5 < \delta < 10^3$, so that the same dm-sized chunks behave in an opposite way at perihelion and in 2014 August (Fulle et al. 2019a). For the high temperatures at perihelion, the dehydration is so fast that the flying and rotating chunks are soon (i.e. within $s_M/D < 4$ h) enveloped by an insulating crust of dried pebbles, which prevents any significant water distributed source in the perihelion coma (Biver et al. 2019), and preserves the chunk ice content into Hapi's fallout. As the chunks land in Hapi's cold polar winter, water vapour sublimating from the chunk interior condenses in its colder crust (De Sanctis et al. 2015). If this frost makes the ice mass fraction in the chunk crust $>10^{-3}$, then inbound to the following perihelion passage the crust becomes active ($D < E$) even if it was inactive at perihelion ($D > E$). In other words the chunks, having the same ice content they had when ejected at the previous perihelion, i.e. $5 < \delta < 10^3$, in 2014 August start again a water-driven erosion, which at low temperatures is not stopped by chunks dehydration.

5 CONCLUSIONS

The proposed activity model, based on gas diffusion inside the cm-sized pebbles making-up a cometary nucleus, explains the 67P activity. Our findings are as follows.

(i) The nucleus erosion rate and the water vapour flux are independent of the refractory-to-water-ice mass ratio, which affects the dehydration rate only.

(ii) The gas pressure inside the pebbles depends on the temperature only, and is >1 kPa at 67P perihelion.

(iii) The water vapour flux depends on the temperature and on the ratio between the monomer and pebble sizes, fitting the 67P water-loss rate data during the northern and southern polar summers if the active 67P surface is ≈5 km^2.

(iv) The smallest and largest ejected dust sizes depend on the nucleus surface temperature and its gradient at depths of a few cm inside the nucleus. Their computed values are consistent with the 67P dust ejection data.

(v) The water-driven nucleus erosion rate depends on the pebble heat conductivity, the average dust bulk density, the pebble heat capacity, and the largest ejected dust size. It is independent of the water vapour flux, implies no nucleus crust and fits the available 67P nucleus erosion data.

(vi) The nucleus dehydration is independent of the erosion rate and depends on the water vapour flux and the nucleus bulk density and refractory-to-water-ice mass ratio.

(vii) The different temperature dependences of the dehydration and erosion rates imply that 67P dm-sized chunks with a constant ice mass fraction behave in opposite ways at ejection and inbound to the following perihelion. At ejection, they are soon enveloped by an insulating crust, preserving most ice up to their fallout in Hapi. Inbound, the water-driven activity at low temperatures triggers a complete erosion of the fallout composed of chunks if their ice mass fraction is >0.1 per cent, explaining the 67P seasonal cycle.

(viii) >95 per cent of the southern pristine 67P nucleus, eroded to depths of ≈10 m (Fulle et al. 2019a; Gundlach et al. 2020), has a refractory-to-water-ice mass ratio >5, confirming independent results (Cambianica et al. 2020).

(ix) In 67P, the southern pristine nucleus is heterogeneous, with most water ice concentrated in <5 per cent of its volume, consistent with observations (Fornasier et al. 2019).

ACKNOWLEDGEMENTS

We thank an anonymous referee for having significantly improved the manuscript, and the *Rosetta* Science Ground Segment at ESAC, the *Rosetta* Mission Operations Centre at ESOC, and the *Rosetta* Project at ESTEC. Part of this research was supported by the ESA Express Procurement (EXPRO) RFP for IPL-PSS/JD/190.2016 and by the Italian Space Agency (ASI) within the ASI-INAF agreements I/032/05/0 and I/024/12/0. JB and BG thank the Deutsche Forschungsgemeinschaft for support under grant BL298/26-1 as part of the international CoPhyLab collaboration. CoPhyLab is jointly funded through DFG (Germany), FWF (Austria), and SNF (Switzerland).

REFERENCES

Biver N. et al., 2019, A&A, 630, A19
Blum J., Gundlach B., Mühle S., Trigo-Rodrigues J. M., 2014, Icarus, 235, 156
Blum J. et al., 2017, MNRAS, 469, S755
Cambianica P. et al., 2020, A&A, in press
De Sanctis M. C. et al., 2015, Nature, 525, 500
Fornasier S. et al., 2015, A&A, 583, A30
Fornasier S. et al., 2019, A&A, 630, A13
Fulle M. et al., 2016, ApJ, 821, 19
Fulle M. et al., 2017, MNRAS, 469, S45
Fulle M. et al., 2019a, MNRAS, 482, 3326
Fulle M., Blum J., Rotundi A., 2019b, ApJ, 879, L8
Gulkis S. et al., 2015, Science, 347, aaa0709
Gundlach B., Skorov Y. V., Blum, 2011, Icarus, 213, 710
Gundlach B., Blum J., Keller H. U., Skorov Y. V., 2015, A&A, 583, A12
Gundlach B., Fulle M., Blum J., 2020, MNRAS, in press
Güttler C. et al., 2019, A&A, 630, A24
Hu X. et al., 2017, MNRAS, 469, S295
Keller H. U. et al., 2015, A&A, 583, A34
Keller H. U. et al., 2017, MNRAS, 469, S357
Kührt E., Keller H. U., 1994, Icarus, 109, 121
Moreno F. et al., 2017, MNRAS, 469, S186
Orosei R., Capaccioni F., Capria M. T., Espinasse S., Federico C., Salomone M., Schwehm G. H., 1995, A&A, 301, 613
Ott T. et al., 2017, MNRAS, 469, S276
Pajola M. et al., 2017, MNRAS, 469, S636
Pätzold M. et al., 2019, MNRAS, 483, 2337
Rotundi A. et al., 2015, Science, 347, aaa3905
Schloerb F. P. et al., 2015, A&A, 583, A29
Shinnaka Y. et al., 2017, AJ, 153, 76
Skorov Y. V., Blum J., 2012, Icarus, 221, 1
Thomas N. et al., 2018, Planet. Space Sci., 164, 19
Tosi F. et al., 2019, Nat. Astron., 3, 649
Zakharov V. V., Ivanovski S. L., Crifo J. F., Della Corte V., Fulle M., Rotundi A., 2018, Icarus, 312, 121

This paper has been typeset from a TEX/LATEX file prepared by the author.

List of astronomical key words (Updated on 2020 January)

This list is common to *Monthly Notices of the Royal Astronomical Society, Astronomy and Astrophysics*, and *The Astrophysical Journal*. In order to ease the search, the key words are subdivided into broad categories. No more than *six* subcategories altogether should be listed for a paper.

The subcategories in boldface containing the word 'individual' are intended for use with specific astronomical objects; these should never be used alone, but always in combination with the most common names for the astronomical objects in question. Note that each object counts as one subcategory within the allowed limit of six.

The parts of the key words in italics are for reference only and should be omitted when the keywords are entered on the manuscript.

General
editorials, notices
errata, addenda
extraterrestrial intelligence
history and philosophy of astronomy
miscellaneous
obituaries, biographies
publications, bibliography
sociology of astronomy
standards

Physical data and processes
acceleration of particles
accretion, accretion discs
asteroseismology
astrobiology
astrochemistry
astroparticle physics
atomic data
atomic processes
black hole physics
chaos
conduction
convection
dense matter
diffusion
dynamo
elementary particles
equation of state
gravitation
gravitational lensing: micro
gravitational lensing: strong
gravitational lensing: weak
gravitational waves
hydrodynamics
instabilities
line: formation
line: identification
line: profiles
magnetic fields
magnetic reconnection
(magnetohydrodynamics) MHD
masers
molecular data
molecular processes
neutrinos
nuclear reactions, nucleosynthesis, abundances
opacity
plasmas
polarization
radiation: dynamics
radiation mechanisms:general
radiation mechanisms: non-thermal
radiation mechanisms: thermal
radiative transfer
relativistic processes
scattering
shock waves
solid state: refractory
solid state: volatile
turbulence
waves

Astronomical instrumentation, methods and techniques
atmospheric effects
balloons
instrumentation: adaptive optics
instrumentation: detectors
instrumentation: high angular resolution
instrumentation: interferometers
instrumentation: miscellaneous
instrumentation: photometers
instrumentation: polarimeters
instrumentation: spectrographs
light pollution
methods: analytical
methods: data analysis
methods: laboratory: atomic
methods: laboratory: molecular
methods: laboratory: solid state
methods: miscellaneous
methods: numerical
methods: observational
methods: statistical
site testing
space vehicles
space vehicles: instruments
techniques: high angular resolution
techniques: image processing
techniques: imaging spectroscopy
techniques: interferometric
techniques: miscellaneous
techniques: photometric
techniques: polarimetric
techniques: radar astronomy
techniques: radial velocities
techniques: spectroscopic
telescopes

Astronomical data bases
astronomical data bases: miscellaneous
atlases
catalogues
surveys
virtual observatory tools

Software
software: data analysis
software: development
software: documentation
software: public release
software: simulations

Astrometry and celestial mechanics
astrometry
celestial mechanics
eclipses
ephemerides
occultations
parallaxes
proper motions
reference systems
time

The Sun
Sun: abundances
Sun: activity
Sun: atmosphere
Sun: chromosphere
Sun: corona
Sun: coronal mass ejections (CMEs)
Sun: evolution
Sun: faculae, plages
Sun: filaments, prominences
Sun: flares
Sun: fundamental parameters
Sun: general
Sun: granulation
Sun: helioseismology
Sun: heliosphere
Sun: infrared
Sun: interior
Sun: magnetic fields
Sun: oscillations
Sun: particle emission
Sun: photosphere
Sun: radio radiation
Sun: rotation
(Sun:) solar–terrestrial relations
(Sun:) solar wind
(Sun:) sunspots
Sun: transition region
Sun: UV radiation
Sun: X-rays, gamma-rays

Planetary systems
comets: general

comets: individual: . . .
Earth
interplanetary medium
Kuiper belt: general

Kuiper belt objects: individual: . . .
meteorites, meteors, meteoroids
minor planets, asteroids: general
minor planets, asteroids: individual: . . .
Moon
Oort Cloud
planets and satellites: atmospheres
planets and satellites: aurorae
planets and satellites: composition
planets and satellites: detection
planets and satellites: dynamical evolution and stability
planets and satellites: formation
planets and satellites: fundamental parameters
planets and satellites: gaseous planets
planets and satellites: general

planets and satellites: individual: . . .
planets and satellites: interiors
planets and satellites: magnetic fields
planets and satellites: oceans
planets and satellites: physical evolution
planets and satellites: rings
planets and satellites: surfaces
planets and satellites: tectonics
planets and satellites: terrestrial planets
planet–disc interactions
planet–star interactions
protoplanetary discs
zodiacal dust

Stars
stars: abundances
stars: activity
stars: AGB and post-AGB
stars: atmospheres
(stars:) binaries *(including multiple)*: close
(stars:) binaries: eclipsing
(stars:) binaries: general
(stars:) binaries: spectroscopic
(stars:) binaries: symbiotic
(stars:) binaries: visual
stars: black holes
(stars:) blue stragglers
(stars:) brown dwarfs
stars: carbon
stars: chemically peculiar
stars: chromospheres
(stars:) circumstellar matter
stars: coronae
stars: distances
stars: dwarf novae
stars: early-type
stars: emission-line, Be
stars: evolution
stars: flare
stars: formation
stars: fundamental parameters
(stars:) gamma-ray burst: general
(stars:) **gamma-ray burst: individual: . . .**
stars: general
(stars:) Hertzsprung–Russell and colour–magnitude diagrams
stars: horizontal branch
stars: imaging
stars: individual: . . .
stars: interiors

stars: jets
stars: kinematics and dynamics
stars: late-type
stars: low-mass
stars: luminosity function, mass function
stars: magnetars
stars: magnetic field
stars: massive
stars: mass-loss
stars: neutron
(stars:) novae, cataclysmic variables
stars: oscillations *(including pulsations)*
stars: peculiar *(except chemically peculiar)*
(stars:) planetary systems
stars: Population II
stars: Population III
stars: pre-main-sequence
stars: protostars
(stars:) pulsars: general
(stars:) **pulsars: individual: . . .**
stars: rotation
stars: solar-type
(stars:) starspots
stars: statistics
(stars:) subdwarfs
(stars:) supergiants
(stars:) supernovae: general
(stars:) **supernovae: individual: . . .**
stars: variables: Cepheids
stars: variables: Scuti
stars: variables: general
stars: variables: RR Lyrae
stars: variables: S Doradus
stars: variables: T Tauri, Herbig Ae/Be
(stars:) white dwarfs
stars: winds, outflows
stars: Wolf–Rayet

Interstellar medium (ISM), nebulae
ISM: abundances
ISM: atoms
ISM: bubbles
ISM: clouds
(ISM:) cosmic rays
(ISM:) dust, extinction
ISM: evolution
ISM: general
(ISM:) HII regions
(ISM:) Herbig–Haro objects

ISM: individual objects: . . .
(except planetary nebulae)
ISM: jets and outflows
ISM: kinematics and dynamics
ISM: lines and bands
ISM: magnetic fields
ISM: molecules
(ISM:) photodissociation region (PDR)
(ISM:) planetary nebulae: general
(ISM:) **planetary nebulae: individual: . . .**
ISM: structure
ISM: supernova remnants

The Galaxy
Galaxy: abundances
Galaxy: bulge
Galaxy: centre
Galaxy: disc
Galaxy: evolution
Galaxy: formation
Galaxy: fundamental parameters
Galaxy: general
(Galaxy:) globular clusters: general
(Galaxy:) **globular clusters: individual: . . .**
Galaxy: halo
Galaxy: kinematics and dynamics
(Galaxy:) local interstellar matter
Galaxy: nucleus
(Galaxy:) open clusters and associations: general
(Galaxy:) **open clusters and associations: individual: . . .**
(Galaxy:) solar neighbourhood
Galaxy: stellar content
Galaxy: structure

Galaxies
galaxies: abundances
galaxies: active
galaxies: bar
(galaxies:) BL Lacertae objects: general
(galaxies:) **BL Lacertae objects: individual: . . .**
galaxies: bulges
galaxies: clusters: general

galaxies: clusters: individual: . . .
galaxies: clusters: intracluster medium
galaxies: disc
galaxies: distances and redshifts
galaxies: dwarf
galaxies: elliptical and lenticular, cD
galaxies: evolution
galaxies: formation
galaxies: fundamental parameters
galaxies: general
galaxies: groups: general

galaxies: groups: individual: . . .
galaxies: haloes
galaxies: high-redshift

galaxies: individual: . . .
galaxies: interactions
(galaxies:) intergalactic medium
galaxies: irregular
galaxies: ISM
galaxies: jets
galaxies: kinematics and dynamics
(galaxies:) Local Group
galaxies: luminosity function, mass function
(galaxies:) Magellanic Clouds
galaxies: magnetic fields
galaxies: nuclei
galaxies: peculiar
galaxies: photometry
(galaxies:) quasars: absorption lines
(galaxies:) quasars: emission lines
(galaxies:) quasars: general

(galaxies:) **quasars: individual: . . .**
(galaxies:) quasars: supermassive black holes
galaxies: Seyfert
galaxies: spiral
galaxies: starburst
galaxies: star clusters: general

galaxies: star clusters: individual: . . .
galaxies: star formation
galaxies: statistics
galaxies: stellar content
galaxies: structure

Cosmology
(cosmology:) cosmic background radiation
(cosmology:) cosmological parameters
(cosmology:) dark ages, reionization, first stars
(cosmology:) dark energy
(cosmology:) dark matter
(cosmology:) diffuse radiation
(cosmology:) distance scale
(cosmology:) early Universe
(cosmology:) inflation
(cosmology:) large-scale structure of Universe
cosmology: miscellaneous
cosmology: observations
(cosmology:) primordial nucleosynthesis
cosmology: theory

Resolved and unresolved sources as a function of wavelength
gamma-rays: diffuse background
gamma-rays: galaxies
gamma-rays: galaxies: clusters
gamma-rays: general
gamma-rays: ISM
gamma-rays: stars
infrared: diffuse background
infrared: galaxies
infrared: general
infrared: ISM
infrared: planetary systems
infrared: stars
radio continuum: galaxies
radio continuum: general
radio continuum: ISM
radio continuum: planetary systems
radio continuum: stars
radio continuum: transients
radio lines: galaxies
radio lines: general
radio lines: ISM
radio lines: planetary systems
radio lines: stars
submillimetre: diffuse background
submillimetre: galaxies
submillimetre: general
submillimetre: ISM
submillimetre: planetary systems
submillimetre: stars
ultraviolet: galaxies
ultraviolet: general
ultraviolet: ISM
ultraviolet: planetary systems
ultraviolet: stars
X-rays: binaries
X-rays: bursts
X-rays: diffuse background
X-rays: galaxies
X-rays: galaxies: clusters
X-rays: general
X-rays: individual: . . .
X-rays: ISM
X-rays: stars

Transients
(transients:) black hole mergers
(transients:) black hole - neutron star mergers
(transients:) fast radio bursts
(transients:) gamma-ray bursts
(transients:) neutron star mergers
transients: novae
transients: supernovae
transients: tidal disruption events